

ARTICLE

Fast Sonochemical Exfoliation of Hematene type Sheets and Flakes from Hematite Nanoarchitectures Shows Enhanced Photocurrent Density

Received 00th January 20xx,
Accepted 00th January 20xx

DOI: 10.1039/x0xx00000x

Purvika Agarwal^a, Debajeet K. Bora^{a*†}

Here, we describe the exfoliation of 2D Hematene single layer from a Hematite nanoparticle-based nanoarchitectures obtained by a water-mediated synthesis route with the ultrasonication method in a brief period which is 5 min. The Hematene obtained shows the fine structure of honeycomb lattice resembling the Hematite hexagonal crystallographic pattern. Here, we found that the ultrasonicated Hematite film with Hematene flakes shows enhanced current density than the pristine Hematite film which can be extended further to increase the efficiency of well-performing or champion photoanode for the artificial photosynthesis application. Besides this, a new photocurrent transient spike is obtained, which we ascribed as the generation of the sub-surface state by Hematene flakes. Followed by this, we have also deciphered a qualitative predictive mechanism for the fast exfoliation of Hematene in which surface energies and hydroxylation of crystal facets are proposed to be the factor responsible for the quick exfoliation process.

Introduction

The emergence of 2D materials by exfoliation techniques finds paramount importance in the current advent of materials chemistry. The importance of the same arises due to its promising properties for various applications. In this regard, Both graphene and metal chalcogenides are studied and applied broadly. However, metal oxides based 2D materials still need further research to decipher its role in various application.

The first scotch tape-based exfoliation of 2D materials from carbon-based allotrope Graphite leads to the discovery of Graphene, and it pushes a new regime of materials research into tremendous applications mostly for electronics device and quantum physics study [1]. The liquid-based exfoliation of layered materials provides high surface area results in enhanced optical and electrochemical properties, and it is possible to exfoliate them into nanosheets due to the weak out-of-plane bonding [2]. With regards to this, chemical exfoliation of metal carbides forms 2D transition metal carbide layers known as Mxene, and it finds various application from electromagnetic shielding to energy conversion and storage application [3]. Not only Mxene, but other 2D materials such as phosphorene, transition metal chalcogenides are also well studied for their diverse application [4 - 8]. Besides these, recently interest rises for the development of 2D metallene nanomaterials such as silicene, antimonene, germanene, stanene [9]. Within this

category, the single layer of PdTe shows polar metal characteristics, which is made by electrostatic doping and proven by first-principle calculations [10]. These materials are Van der Waals solids, due to the force existing in between the interlayers in bulk material, as observed in the case of Graphene [11]. Not only these, but oxides and their layered double hydroxides also belong to 2D materials. Several metal oxides such as TiO₂, WO₃, ZnO and Co₃O₄, have been rigorously studied and have been converted to their two-Dimensional forms in the form of layered double hydroxide and shows many different electrochemical properties [12]. A recent candidate of 2D copper (II) oxide nanosheet [13] is prepared by the surface Sulphur functionalization, which shows semiconductor-conductor transition. Besides these, Iron oxides and their analogues possess widespread applications in the diverse fields of catalysis [14], magnetic storage media [15], gas sensing, Lithium-ion batteries [16] and other biological applications [17]. Hematite (α -Fe₂O₃), being an n-type semiconductor, possesses excellent stability and an appropriate bandgap, making it well known for artificial photosynthesis application [18]. However, iron oxide-based 2D materials such as layered double hydroxide which is generally not photoactive and are used in electrocatalytic hydrogen production due to the high surface area and low overpotential and fast water oxidation kinetics derived by a higher catalytic turnover process for the oxygen evolution reaction [19]. The photoactive 2D exfoliated layers of the Hematite semiconductor has not been explored.

With the discovery of sonochemical route or the ultrasonication method, various nanostructured materials with reasonable control over size, morphology and crystallographic structure can be formed. Cavitation and Nebulization are primary physical phenomena associated with the ultrasonic synthesis of nanomaterials [20]. The application of the same for the

^a Centre for Nano and Material Sciences, JAIN (Deemed – to – be University), Jain Global Campus, Bangalore 562112, India

† corresponding author: Debajeet K. Bora, Ph.D. E-Mail: debajeet.bora@jainuniversity.ac.in, debajeet1@outlook.com

Electronic Supplementary Information (ESI) available: AFM data statistics, FESEM images, Size distribution, XPS survey scan, Fe2p core level scan and fitted spectrum, UV-vis spectrum of Hematene extracts.

exfoliation of the 2D single layer from metal oxides into Graphene like sheet and flakes [21] is an exciting area of materials development. Balan et al. reported a sonochemical route for the exfoliation of 2D Hematite from geological Iron Ore, called as *Hematene*. The Hematene layer forms by the breaking of strong covalent bonds between the Fe-O layers of Hematite crystal by the ultrasonication process [22]. They used the sheet-like layer for the TiO₂ photoelectrode sensitization to measure the photocurrent density with an application toward water-splitting mediated hydrogen formation. The Hematene obtained also shows ferromagnetic order while Hematite usually shows antiferromagnetic behaviour. Note that Hematene are non-Van der Waals materials, and it shows exotic magnetic properties with a magnetic moment of 4μ_B per atom according to a recent DFT study, followed by this Hematene surface functionalization on Stanene converts the same into ferrimagnets [23]. Hematene, as a non-van der Waals 2D material is also chemically stable in the ambient conditions due to its oxygen passivation [24] and next, Hematene based heterostructure (Hematene / BaTiO₃) is also developed to tune the magnetic properties [25]. Not only magnetism, but Hematene also find suitable application in the biomedical sector and associated energy research with the development of it for glucose sensing application with its electrocatalytic application followed by the development of a biofuel cell operated by glucose [26]. For the oxygen evolution electrocatalysis study, recently defect enriched Hematene is shown a current density of 10 mA/cm² at 0.250 V overpotential [27]. The energy storage outlook of this material is recently taken into consideration and is published elsewhere [28].

The usual exfoliation time in the studies mentioned above, for instance, from geographical ores is quite long as the Fe-O strong bonding will not allow the exfoliation process efficiently [22]. However, exfoliation of Hematene from Hematite nanoparticle and their thin film can be an additional advantage concerning surface energies of different crystalline facets within different morphological variants of iron oxide [29]. Hence, the development of a fast exfoliation method is the motivation of the current study. Also, how ultrasonication helps in the formation of Hematene flakes from a nanoparticulate thin film is not explored to the best of our knowledge—another critical aspect in this regard, the effect of Hematene on the photocurrent density after ultrasonic exfoliation. The application of Hematene to direct photoanode development for solar fuel research will be the preliminary understanding in the current study.

Results and discussion

The reaction of iron trichloride with water is termed as forced hydrolysis [Figure 1-I], and this yields many different morphologies. In this case, the influence of urea is to control the

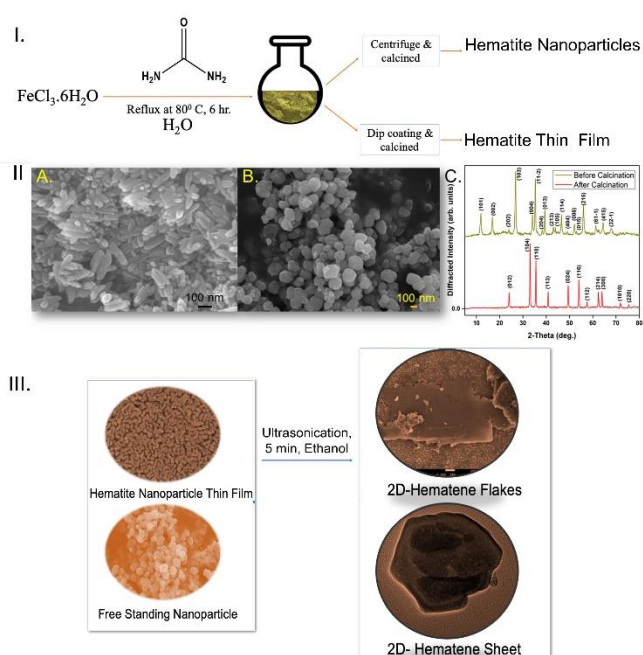


Figure 1: I. One-step synthesis of iron oxyhydroxide precursors in water to make Hematite nanoparticles clusters and films by the centrifugation and dip coating methodology followed by thermal treatment; II. A. FESEM image of iron oxyhydroxide rods like particles (akaganeite phase) as confirmed by the X-ray diffraction; B. FESEM image of the heat-treated akaganeite rods shape particles to form Hematite spherical nanoparticles with the mean size distribution of 115 nm; C. Comparison of X-Ray diffraction patterns of akaganeite and Hematite phases shows the removal of different Bragg diffraction peaks after the heat treatment. III. Left: FESEM images of Hematite nanoparticles thin film and free-standing nanoparticles powder and Right: ultrasonication condition in Ethanol to make 2D-Hematene Flakes and single layer Hematene sheet.

the shape of nanoparticles. Here, additives such as urea adsorbed on the specific crystal planes of growing crystals [30]. From the SEM characterization of powders [Figure 1- II], we found that the morphology of the as-prepared powder shows the rod-like pattern, which is a characteristic of the formation of akaganeite rods on top of which Hematite nanoparticle nucleate [31]; which on heat treatment or calcined at 500°C results in cube shape particles. A similar morphological transition and its growth have been reported in earlier literature [32]. The mean particle size of rod shape particles is found to be 34 nm while that of hematite nanoparticles is 115nm [Figure S5]. Next, it is found that Hematite nanoparticles were grown from ferric chloride salt used to be covered by (104) exposed crystallographic planes, which is also confirmed here from the XRD of nanoparticles, where (104) Bragg planes have the maximum XRD peak intensity. The XRD patterns of the sample in their powder form have been illustrated in Figure 1-II C and matched well with the JCPDS no. 34-1266, which is usually indexed for akaganeite (β-FeOOH) phase of iron oxide and upon thermal treatment of it at 500°C, undergoes a phase transformation into Hematite (α-Fe₂O₃). The two prominent peaks (104) and (110), indexed to the JCPDS no. 33-0664, could be understood to grow from (004) and (11-2), while the (104) peak growing with higher intensity compared to (110), which was a common observation in an earlier report [33].

Hematene fabrication and its morphological study with HRTEM

The ultrasonic exfoliation process has been carried out for both Hematite nanoparticle powder and the thin film to get Hematene sheets and flakes, as shown in Figure 1-III in a one-pot setup. We called it as ultrasonic or sonochemical exfoliation because we observed such exotic 2D materials after the ultrasonic preparation of nanopowder suspension in Ethanol for TEM characterization. On ultrasonication for 5 minutes in Ethanol, layers are etched out forming flakes for thin film and sheet-like morphology for nanoparticles. The advantage of our process is the time taken for the completion of the exfoliation. The obtained nanostructures can be directly exfoliated after 5 min of the ultrasonication. While, in regular LPE (liquid phase exfoliation) process, the materials to be exfoliated is kept in the ultrasonication for more than 24 hours. It applies on a case to case basis and already explained in the introduction.

Here, we will first discuss the HRTEM results obtained for the Hematene sheets obtained from nanoparticle to shed light into its structural and morphological characteristics. Afterwards, we will move on to discuss the result obtained from the FESEM investigation of the thin film containing Hematene flakes. Whether these new 2D materials possess any characteristics for photoelectrochemical functionality, we have further studied its detail structural, topological, morphological, optical and surface composition investigation with advanced microscopy as well as spectroscopic and diffraction tools.

Next, to probe the morphologies of nanoparticles, we have performed HRTEM (High-resolution transmission electron microscopy) investigation of ultrasonically dispersed nanoparticles [Figure 2A]. The low-resolution TEM study of nanoparticles shows aggregate like feature morphology resembling a cauliflower type in the first observation. Next, we have found a partially hexagonal sheet-like morphology at 20 nm scale, which on close inspection at higher resolution, shows honeycomb lattice structure usual of Graphene [Figure 2 B- E]. On comparing this morphology with existing literature [20], the terminology of Hematene comes from the fact that a similar type of honeycomb lattice was observed during the ultrasonic exfoliation of naturally available iron ores [20]. It further signifies the first direct exfoliation of Hematene with sonication method within a short period. We called it a fast process, as the time required for the formation of Hematene is 5 min, whereas in other studies it takes a long time (more than 20 hours) to exfoliate the sample [22, 26, 27] which finds an interesting aspect from the processing point of view, and it is first of its kind to the best of our knowledge.

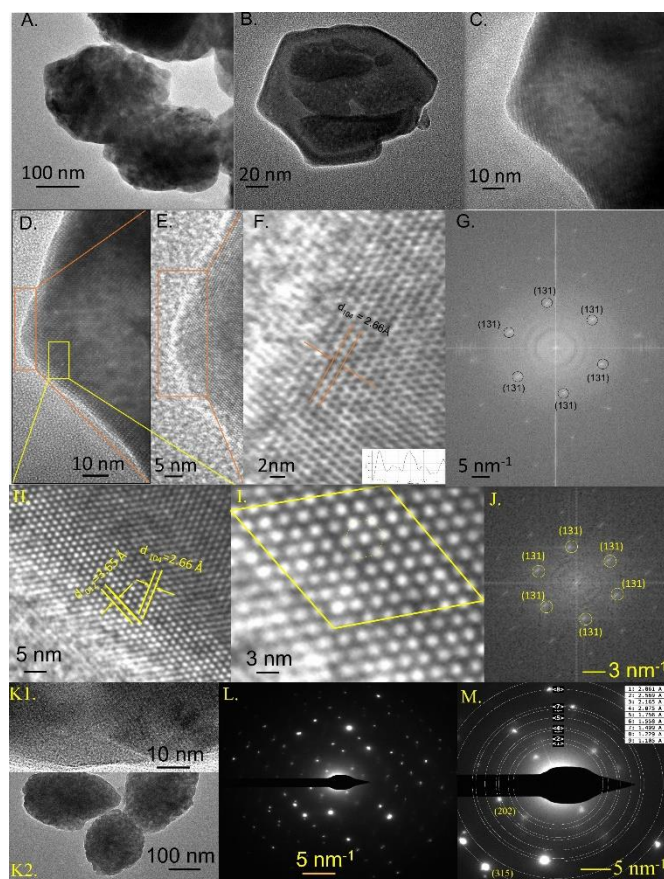


Figure 2: A. Low-resolution TEM imaging of Hematite nanoparticle clusters; B. Low-resolution TEM image of a single-layer exfoliated Hematene sheet; C. HRTEM imaging of one corner of Hematene sheet; D – F: Expanded image view of the edge shows the honeycomb-like structure with d-spacing magnitude closely resembles the Bragg diffraction pattern of Hematite. The existence of honeycomb lattice signifies the Hematene Exfoliation; G: FFT image transformation of image F shows diffraction peaks closely matches to (131) planes of Hematite. H. shows the superlattice pattern of Hematene; I. the nanocrystalline superlattice atomic assembly in a hexagonal order; J. The FFT conversion of E shows the diffraction pattern of single layer Hematene. K1: HRTEM lattice imaging of the edge of the nanoparticle shows lattices fringes; K2: Low-resolution TEM imaging of nanoparticle cluster; L. Selected area electron diffraction (SAED) pattern of the nanoparticle clusters; M. SAED analysis with Fiji TEM package.

Detail atomic structure investigation of Hematene sheet with HRTEM

The atomic structure of the Hematene sheet formed is further investigated by doing lattice imaging of Hematene sheet edges, as shown in Figure 2F. Here, the interlayer spacing between two atomic planes of Hematene is found to be 2.66 Å, which corresponds to (104) planes of Hematite crystallographic structure. The FFT (Fast Fourier Transform) of HRTEM lattice imaging results into the electron diffraction patterns of hexagonal symmetry, as shown in Figure 2G. A similar type of hexagonal symmetry is also observed for Hematene obtained by Balan et al. [22]. It further confirms the Hematene formation, although we do not have direct evidence about the crystallographic projection here to know the basal planes. Whereas, in other studies, it is (001) plane [22]. The indexing of diffraction spots reveal (131) planes with d - spacing value closely matched to the JCPDS pattern of Hematite with rhombohedral crystal system.

Both of these observations are a clear indication of the crystallographic origin of Hematene single layer exfoliated from Hematite lattice with the ultrasonication procedure, and the formation of free-standing 2-D Hematene sheet is well confirmed. We have made another interesting observation here by looking at different edges (yellow rectangular portion) of the Hematene sheet lattice fringes. Here, we have obtained a superlattice arrangement of the atomic assembly in a hexagonal order for the nanocrystallites, as shown in Figure 2H. The d-spacing matches well with (012) Bragg planes, and the plane at a 75° angle is (104). The close look of it reveals an evolutionary pattern of the atomic arrangement in a hexagonal order [Figure 2I]. There are two types of atomic layers observed. The inward layer and outer layers are repeating in ordered manners refer to the formation of a single layer Hematene sheet [22, 27]. The FFT of the corresponding lattice fringes [Figure 2J] also shows the formation of hexagonal spots corresponding to each atom constituting the Hematene crystallographic structure and its repeating in a similar pattern. The FFT diffraction spot corresponds to the (131) planes of Hematite. A similar type of atomic arrangement is observed for the Hematite nanocrystal with bitruncated dodecahedron shape [29].

Next, we have performed HRTEM of nanoparticle clusters in different ROI (region of interest) with the selected area electron diffraction pattern (SAED) to get further details about the atomic arrangement of hematite nanocrystallites from which Hematene is exfoliated. The low-resolution TEM of Hematite nanoparticles (Figure 2 K1) shows again aggregate like features, which on HRTEM shows usual lattice fringes (Figure 2 K2) proving the crystalline nature. The selected area diffraction pattern (SAED) of the crystallites and its analysis (Figure L and M) with Fiji TEM package of Image J shows ring patterns, where ring number 4 and 9 matches with Bragg planes of Hematite (202), (315) respectively. The presence of diffraction spot further confirms the base material from which Hematene is exfoliated is a pure Hematite crystal.

How Hematene forms?

The mechanism of Hematene exfoliation and the process of temporal control lies in the understanding of surface energies of most exposed crystallographic planes is shown in Figure 3. Note that, to understand the same, first we have to know the surface energies of (104) planes in our finding, and the naturally obtain Hematite ores which have basal planes (0001) lying along the foliation plane [34]. Followed by this, we will emphasize the hydroxylation of the Hematite surface. It takes a minute to an hour for the hydroxylation depending on the surface reactivity of each plane. It is a well-established fact that Hematite surface usually contains Fe atoms with unoccupied state and act as Lewis acids and reacts with Lewis bases such as hydroxyl ions via the available electron pair [33]. Due to the same, hydroxyl ions adsorb on the surface of iron oxide via coordination with Fe atoms. In the present study, heat treatment of the

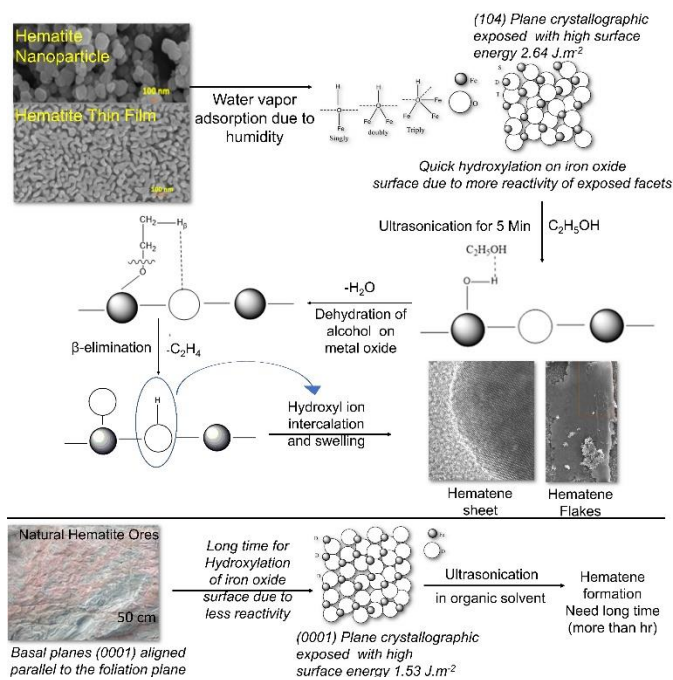


Figure 3: Hematene formation mechanisms from both Hematite nanoparticle and thin film with a comparison to the long duration for exfoliation from naturally abundant Hematite ore.

Akageneite nanorod leads to the formation of Hematite nanoparticle. It removes the surface hydroxyl group and forms water molecule due to the surface condensation, and the same is desorbed later. Now the dehydroxylated Hematite nanoparticle on exposure to ambient temperature due to water vapour, (104) exposed facets as confirmed by the XRD, three types of coordination will be evident based on the earlier study [30]. The hydroxylation of the Hematite surface depends on the surface energies of exposed crystal facets. For instance, the surface energy of (104) plane of nanoparticle described here is around 2.64 J / m² [36] while that of (001) basal planes in case of naturally abundant Hematite ores is 1.53 J/m² [37]. So, hydroxylation time of both cases will differ and will finally affect the exfoliation process run by a secondary process such as ultrasonication and solvent interaction with metal oxide surfaces. In the first report of Hematene fabrication, the exfoliation process taking a long time of the order of 30 hr [22] whereas, in this current study, it just needs 5 min. In our case, this hydroxylation step is faster due to the more exposed (104) plane, leaving the exposed hydroxyl group, which will further react with the absolute alcohol.

The metal oxide is well known for the dehydration of alcohol and beta elimination reaction, in which unsaturated organic compounds such as ethylene get produced according to the literature described elsewhere [38]. Here, alcohol hydrogen atom intercalated to the oxygen of the Fe-O-Fe linkage forming a hydroxyl moiety (O- H) covalent bond between two metal atoms. It takes place on (104) crystal facets leaving stress on the planes, which will finally lead to the formation of Hematene single-layer sheets. It is bound initially by non-van der Waals forces. Besides this, this hydroxyl moiety acts as a knob to control the magnetoelectric coupling in ferroelectrics such as Ca₃Mn₂O₇. It is also formed by hydrogen intercalation and due

to the same antiferromagnetic metal oxides shows ferrimagnetic properties [39]. It is also evident in the case of Hematene, which shows ferrimagnetic behaviour, as stated above [23].

Formation of Hematene Flakes

In the water-mediated synthesis, we have obtained only cauliflower-like particles, but without the formation of nano-octahedron usually obtained in an oleic acid-mediated approach. The homogenous solution mixture is also used for thin-film coating, as shown in Figure 1-I A, which on calcination at 500°C results in a Hematite film by following the procedure described elsewhere [40]. So far, we have described the formation of a free-standing Hematene nanosheet. Nevertheless, to apply them as a functional material, we need a handful of a system where its influence can be observed towards a specific functionality. In this regard, our goal is to use this type of 2D materials towards photoelectrochemical water splitting application. So, to achieve the same, as described above we ultrasonically transform Hematite nanoparticle film [Figure 1-III] into an exfoliated film with the generation of flakes like an object, which we called as Hematene flakes by the 2D morphological characteristics as observed by FESEM. From here on, we will designate both Hematite films before and after ultrasonication as B.S. and A.S. On the other hand, the free-standing Hematene sheets are challenging to apply directly for device application.

FESEM and EDX investigation of Hematene flakes containing thin film

We have performed field emission scanning electron microscopy (FESEM) studies of Hematene flakes to observed the morphology and its 2D type structure. It is followed by a detail compositional characteristic of the Hematene flakes to confirm the presence of Fe and O only, which composed the usual iron oxide bulk counterpart. The morphology of calcined Hematite thin films (A.S. and B.S.), before and after ultrasonication, has been studied and their images are presented in Figure 4 A and B, respectively. The FESEM image of the B.S. [Figure 4A] obtained by dip-coating methodology as described in our earlier study [41], shows anisotropic nanoparticles with the fusion of two nanoparticles in an elongated pattern. The A.S. morphology is shown in the FESEM image [Figure 4 B]. Here, the morphology of the particle remains the same but the exfoliation results in a more porous like features. In B.S.; particles have been uniformly deposited and possess smooth surface as confirmed from the FESEM image of the thin film. While upon sonication, in figure 4B, the smooth surface was converted to rough, as the particles from the film etched out.

Further, in Figure 4C, we have shown a FESEM image representing 2D flakes like structure is formed on top of A.S. The flakes are also deposited in a free-standing manner on a

coverslip [Inset; Figure 4B]. The purpose is to understand that the 2D layer like materials is originated from base Hematite nanoparticles. Next, to determine the precise thickness of the obtained Hematene sheets and flakes, we have 3D transformed their corresponding HRTEM and FESEM images with Image J. From the result obtained as shown in figure S4, it is evident that the Hematene sheet obtained thickness is around 20 nm after carefully looking in the scale bar intensity of spectrum LUT images in the right side of the image. Similarly, the thickness of Hematene flakes [Figure 4 D] is found to be 200 nm. Note that a precise analysis of Hematene sheet thickness needs molecular dynamics simulation as described elsewhere [22].

Further, to rule out the presence of other elements or any external foreign objects such as dust, we have made the EDX mapping and line scan of the flakes structures. Here, EDX mapping [Figure 4 E] study confirms the distribution of Fe and O elements besides Sn, which mostly come from the substrate. Note that, we have F- doped SnO₂ as a substrate to deposit the Hematite film. The line

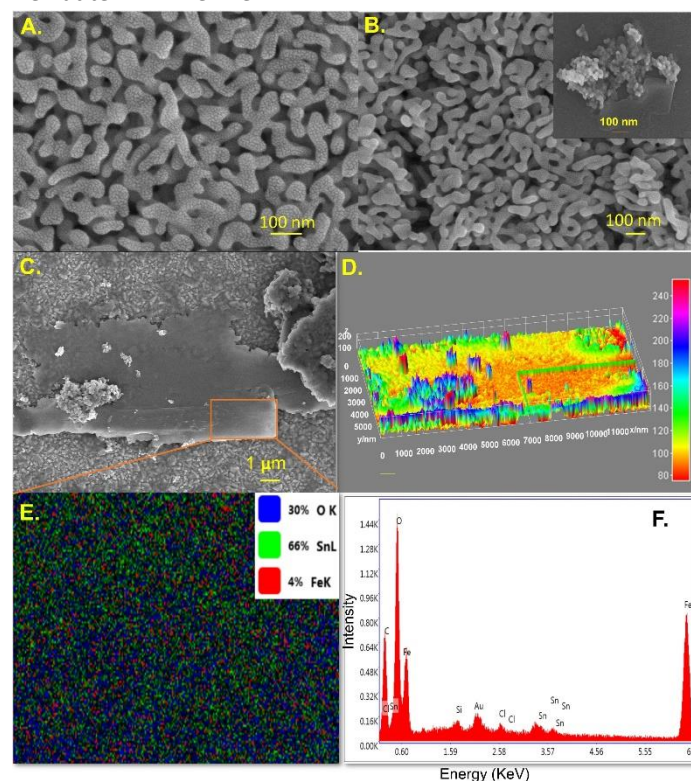


Figure 4: A. FESEM image of Hematite thin films; B. the FESEM image of the film after the ultrasonication process; Inset shows etched out flakes after drop-casting on a coverslip; C. FESEM images of the 2D flakes obtained after the ultrasonication process; D. 3D image transformation of FESEM images with spectrum LUT representation of Hematene flakes by Image J; E. The composition of the 2D flakes is studied with EDX mapping, and it shows the distribution of Fe and O elements further confirming the origin of the flakes to Hematite, F. The EDX scan of the Hematite thin film shows Fe and O elements.

scan analysis also confirms the presence of the same elements. From this observation, it is concluded that due to the ultrasonication process, flakes like 2D materials are etched out, and this structure is made of Hematene as confirm from the EDX mapping with a transparent nature showing the underneath FTO crystal. The usual Hematite SEM never show this kind of morphology. The atomic % wise distribution of elements [Fe=

4%, O = 30%] confirms the stoichiometry of the Hematite. In this case, the formation of the hematite phase by XRD investigation directly confirms the $\alpha\text{-Fe}_2\text{O}_3$ stoichiometry (Hematite phase) of the materials as described below.

Next, we have also carried out the AFM measurement of Hematene sheet and flakes to determine their thicknesses. However, the result obtained [figure S1] does not reveal the image as obtained during the TEM and FESEM investigation. To determine the thickness of corresponding hematite nanoparticles, sheet and films thereof, we have plotted the RMS roughness of the surface for each sample. The result obtained is shown in figure S2. For the Hematene sheet, the surface roughness decreases while for Hematene flakes, it increases after the ultrasonication process. We have compared the high magnification FESEM of free-standing Hematene flakes with the one obtained on the thin film [Figure S 11] at a bulk level. Here, the surface roughness in both cases does not show any significant difference, and it appeared to be smooth on close inspection of FESEM images. At the surface atomic scale, AFM scan of Hematene flakes carried out above shows an increase in the surface roughness after the ultrasonication processes. Note that, Hematene flakes reported here are from the same samples.

Optical and Crystallographic properties of Hematene flakes and sheets

To understand further, we investigated the optical property of Hematene sheet, flakes and film before and after ultrasonication (B.S. and A.S.) with a focus on the light absorption characteristics and electronic properties. The same will be studied by the analysis of the shifting of absorption maxima λ_{max} and calculation of the energy bandgap (E_g) with Tauc methodology for indirect bandgap semiconductors. The understanding of Hematene flakes light absorption property is essential to decipher its role in the photoelectrochemical properties. For the same, we have carried out the optical property studies of both free-standing Hematene sheet and flakes on film with UV-Vis spectroscopy in both liquid and solid-state condition. For the free-standing Hematene sheet, we have taken the exfoliated Hematite nanoparticle solution obtained by the ultrasonication process. Besides these, we have also studied the exfoliated Hematene or flakes form in solution. For the flakes like Hematene, the etched-out particles were used for UV-Vis analysis by making an ethanol dispersion. Note that after exfoliation of thin film by ultrasonication, we have obtained reddish-brown dispersion which we believe the presence of Hematene flakes along with exfoliated nanoparticle from the film.

The UV-Vis spectra of all samples including free-standing Hematene sheet, flakes, A.S. and B.S are shown in Figure 5 A. We have observed the absorption intensity maintain its maxima at 550 nm (λ_{max}) for both Hematene flakes and Hematene sheet concerning absorption spectra of both A.S. and B.S; where

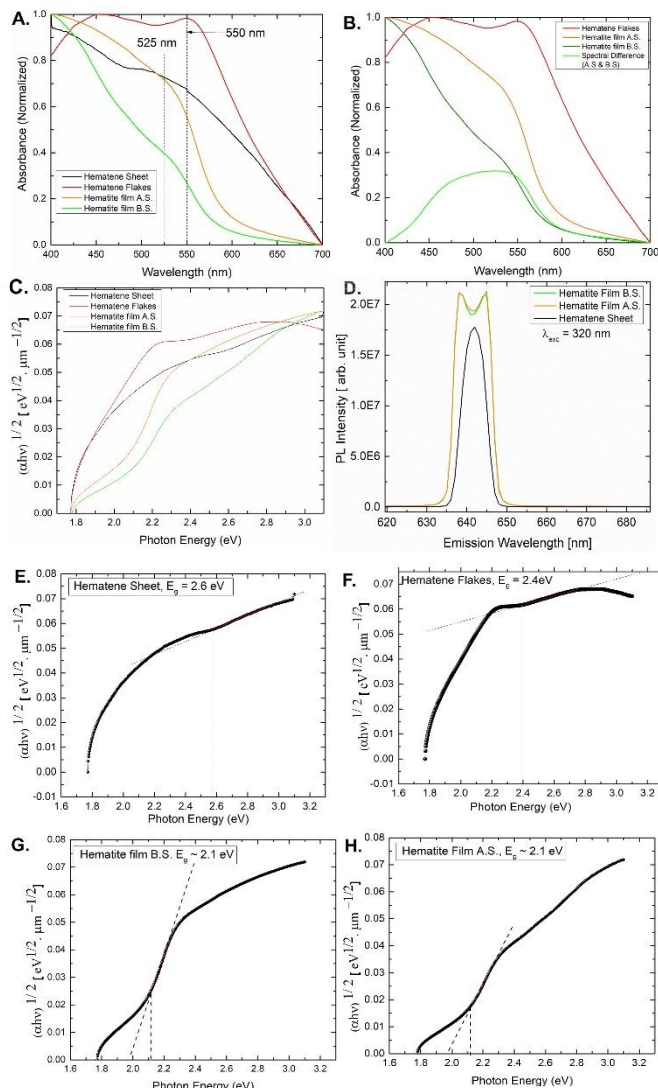


Figure 5: A. The comparative U.V. - Vis absorption spectra's of Hematene sheet and Hematene Flakes with the Hematite film before and after ultrasonication; B. U.V. -Vis absorption spectra of Hematite thin films before and after ultrasonication and the spectral difference shows the Hematene absorbance peak similar to Hematene flakes shape, C. Tauc plots of Hematene sheet, flakes and Hematite thin film after and before ultrasonication, D. Photoluminescence emission spectra of Hematene sheet concerning the hematite film A.S. and B.S.; E - H. Energy band gap values calculated from respective Tauc plots of Hematene sheet and Hematene Flakes with the Hematite film before and after ultrasonication considering it as an indirect bandgap semiconductor.

it is shifted towards shorter wavelength $\lambda_{\text{max}} = 525$ nm. It will be discussed in the next section. In contrast, additional absorption band appears at 400-450 nm in all cases, which is a characteristic spectral signature of Hematite UV-Vis spectrum, where two absorption band at 400 nm and 550 nm is typically observed [30]. Hematene flakes show the maximum absorption intensity of all cases, which makes it a good absorber material for photoanode development. Next, we have seen that its peak intensity decreases down at 450 nm in comparison to Hematene sheet, which still absorbed photons below this range. It might be due to the concentration difference of the materials understudied as the flakes like materials forms less concentrated solution due to less density of flakes in comparison to the sheet, which is easy to exfoliate into ethanol solution and form a reasonably concentrated solution. However, a detail electronic calculation understanding is needed here from the density functional theory to understand

these sharp differences. It is also evident that the light absorption intensity profile in the range from 550 nm - 700 nm is following different trend than that of the B.S. and A.S. to be discussed next. It is an impressive result considering the fact of the panchromatic light-harvesting ability of this particular Hematite based 2D materials, which is a new finding to the best of our knowledge. It can be further extended in the interaction study of free-standing Hematene sheet with light-harvesting proteins and pigments in hybrid organic optoelectronics.

Next, we have carried out the UV-Vis absorbance studies of Hematite films both before and after ultrasonication (B.S. and A.S.) in solid-state condition (Figure 5B). The role of Hematene flakes obtained in the ultrasonicated film as mentioned above in the photoanode functionality for light-harvesting is the primary criteria here is to evaluate. The UV-Vis absorption spectrum of B.S. and A.S. shows the λ_{\max} at 525 nm. Besides this, the absorbance intensity is more for the A.S. than B.S. Whether this increase in absorbance directly influences from the Hematene flakes, we have plotted the UV-Vis absorbance spectrum of Hematene flakes with that of A.S. and B.S. followed by a differential spectrum between A.S. and B.S. [Figure 5B] to understand it further. The differential spectrum shows the same shape of the absorption spectrum as that of Hematene flakes. The shapes resemble the convoluted pattern of Hematene flakes absorbance spectra, which further confirms

fractions. From here, it is concluded that the spectral shape is independent of the size of the nanosheets from the suspension. To understand it better in terms of electronic structure, we have plotted the Tauc plots, as shown in Figure 5. [C, E- H] of all samples by considering the indirect bandgap of Hematite. Here, it is evident that the Tauc profile for both Hematene sheet and flakes deviating from the standard pattern of Tauc plots for B.S. and A.S. From here, it reveals that the energy bandgap (E_g) of (Hematene sheet = 2.6 eV & flakes = 2.4 eV) significantly differs from that of pristine Hematite. In comparison, Hematene flakes containing film (A.S.) shows the usual band gap value of 2.1 eV. Note that the Hematite has an indirect phonon-assisted bandgap transition value of 1.9-2.2 eV [42]. The associated shift in bandgap energy is attributed to the blue shift of the small Hematene nanostructures. Hematene formation results in the raise of the conduction band and lowering of valence band, thereby result in broader band gap value and blue shift of the absorption edge [43]. The same result agrees with the band gap value of the Hematene obtained by the ultrasonication of natural Hematite ores [22].

Next, we have presented the photoluminescence spectrum, as shown in Figure 5D. Here, on excitation with 320 nm wavelength, we have observed the emission spectra at 640 nm. Here for both Hematite film A.S. and B.S., the emission peak shows a doublet pattern while that of Hematene sheet shows singlet. It is the size of iron oxide nanoparticle controls a common observation found in the X-ray emission spectra [44].

The scattering contribution and its quantitative analysis are also understood here to take into account the scattering contribution on the optical properties. It is carried out by measuring the diffuse reflectance spectrum of Hematite Film B.S. and A.S. followed by the Hematene sheet. Here we have applied the Kubelka-Munk function to the diffuse reflectance spectrum with the following equation:

$$f(R) = \frac{(1-R)^2}{2R} = k/s$$

Where R is the diffuse reflectance of the layer relative to a standard such as magnesium oxide, k is the molar absorption coefficient, and s is the scattering coefficient of the sample. The diffuse reflectance spectra of all samples are shown in figure 6 A. We have observed similar type of diffuse reflectance pattern for both Hematite Film A.S. and Hematene sheet while Hematite film B.S. shows high reflectance till 600 nm, afterwards reflectance getting lower till 400 nm. To understand the same, we have plotted the scattering coefficient (s) and found that it varies significantly for pristine Hematite film, but for Hematite film A.S. and Hematene sheet, the pattern looks almost same [Figure 6B]. It further confirms that the morphology of Hematene sheet and flakes are the same as the scattering contribution are almost similar for both cases whether film or dispersion. For pristine hematite film, the scattering gets higher from 550 nm onwards. Hence the absorbance changes due to different scattering coefficient for all samples. It is also found that the scattering and absorption coefficients of Hematite changes for morphology and size of the nanoparticle [30].

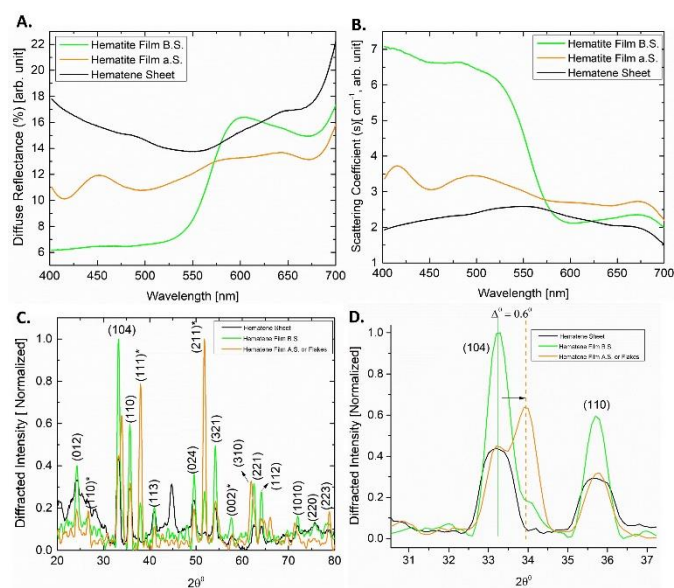


Figure 6: A. The diffuse reflectance spectra of Hematene sheet and corresponding film before and after the ultrasonication process; B. The scattering coefficient (S) calculated from Kubelka-Munk function for all films and sheet; C. The thin-film X-ray diffractogram of Hematene sheet and hematite film A.S. (contains flakes) and B.S.; D. Expanded comparative view of the (104) Bragg diffraction peaks of all materials

the formation of it on the pristine Hematite film after ultrasonication. Whether the size of Hematene flakes or sheet has any influence on the spectral shape, we have accordingly isolated three fractions of Hematene sheet suspension and measure their UV-Vis spectra. It is shown in figure S10. From the result obtained, it is evident that the shape of the absorption spectrum for λ_{\max} does not change irrespective of the isolated

From our previous study [40], it is evident that the forced hydrolysis of iron chloride salts in the presence of urea always results in maximum peak intensity for (104) Bragg planes as confirmed by XRD. Here, we have studied the detail crystallographic properties of the Hematene flakes. We have carried out the thin film XRD investigation of all three materials such as Hematene sheet, hematite film B.S. and hematite film A.S. As shown in figure 6 C; we found that all the Bragg diffraction peak shows the typical crystallographic structure of Hematite according to the JCPDS pattern. The diffracted intensity of (110) plane decreases after the ultrasonication process for Hematite Film A.S. Next on expanding the (104) and (110) peak [Figure 6D], it is evident that a new peak splitting has been observed for (104) plane in case of Hematite film A.S. The (104) peak intensity after the ultrasonication process decreases while a new peak appeared at 0.6° from the original Bragg angle. It further signifies the hydroxyl ion intercalation along the (104) peak as described in the mechanism [Figure 3]. A similar type of peak splitting is observed in the in-situ X-ray diffraction pattern of chloroaluminate ion intercalation in aluminium batteries [45].

Surface properties of Hematene flakes and sheet from XPS study (X-Ray photoelectron spectroscopy)

The XPS (X-Ray photoelectron spectroscopy) is performed for hematite nanoparticle film obtained from the heat treatment of rod-shaped particle, the film after the ultrasonication process and Hematene sheet (dispersion) followed by a control measurement of substrate FTO (Fluorine doped tin oxide) on which hematite film is deposited. The survey scan of all samples is shown in figure S6. Here, the peak obtained is due to O1s and Fe2p signal mostly except for the Hematene sheet or dispersion. The surface atomic composition of all films is shown in table S2. The composition shows the variation in atomic ratio both before and after ultrasonication.

The O1s core level spectrum of all samples is shown in Figure 7 A. The first peak at 529 eV comes from the hematite lattice while a second peak at 532 eV is considered as a defect peak, which is usual of Hematene electronic structure as mentioned elsewhere [22]. The oxygen 1s core level scan of FTO reveals a peak at around 531.70 eV [46], and this peak deviates itself from the defect mediated peak. The Fe2p core level scan of hematite thin film B.S. and A.S. is shown in Figure 7 B. Here, the change in oxidation state has not been observed after the ultrasonication process. Next, we have fitted the oxygen 1s core level spectrum with multiple peaks

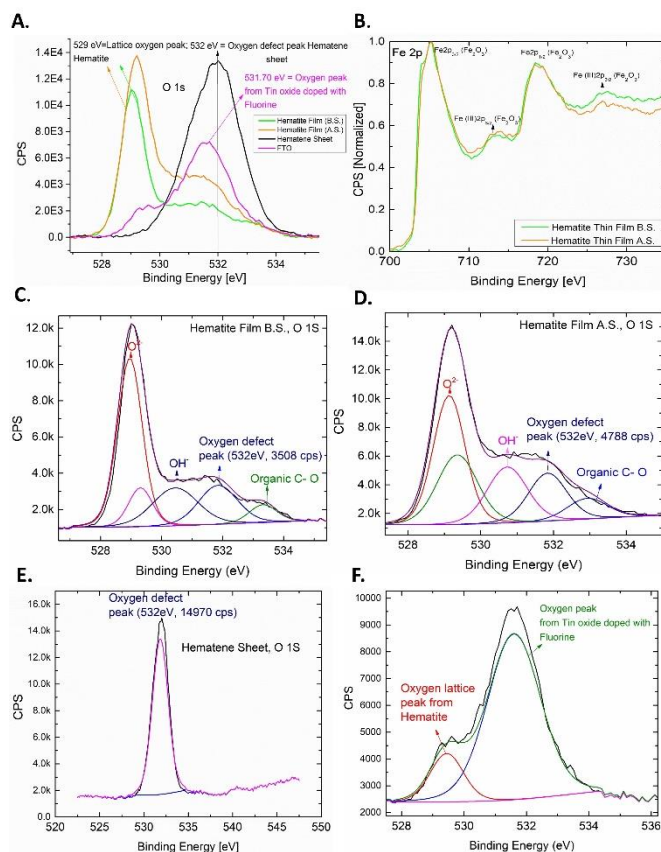


Figure 7: A. The comparison of O 1s core-level XPS spectrum of Hematene sheet, FTO (Fluorine doped tin oxide), hematite film B.S. and A.S.; B. Comparison of the Fe2p core levels can of all films; C. Deconvoluted O1s core level XPS spectrum showing the defect peak at 532 eV for Hematite film B.S.; D. Deconvoluted O1s core level XPS spectrum showing the enhanced intensity of defect peak at 532 eV for Hematite film A.S.; E. The fitted O1s core level spectrum of Hematene Sheet F. The fitted O1s XPS spectrum of FTO substrate shows a slight increase in oxygen lattice peak intensity from Hematite due to cross coating of Hematite to the free area.

deconvolution [Figure 7 C - F]. For both hematite films, B.S. and A.S.; the lattice peak, as mentioned above, is constituted of O^{2-} and OH^- signatures followed by the formation of oxygen defect signature at 532 eV. Next, it is observed that the intensity of this particular signature is more in hematite film A.S. concerning Hematite film B.S. further confirming the formation of Hematene flakes. Next, we have deconvoluted the O1s peak from Hematene sheet, and it signifies a pure defect-related peak at 532 eV. Finally, the fitting of O1s spectrum reveals also a small spectral weight at 529 eV pointing towards the presence of Hematite coating.

Photoelectrochemical properties of Hematene flakes containing thin film

Photoelectrochemical properties of the pristine Hematite film and the corresponding Hematene flakes exfoliated thin film

We have applied Hematene flakes exfoliated Hematite film as discussed in the FESEM investigation section to check for the photoelectrochemical application due to its light absorption properties as discussed above. We have not performed any measurement for the sheet-like Hematene materials as it is challenging to make a stable dispersion. There is a way to sensitize any photoanode materials with these Hematene materials like Graphene sensitized photoanode encountered in many studies. With this regards, Hematene coated titanium dioxide is published elsewhere as a sensitizing material [22]. Also, its application for the photoelectrochemical water splitting reaction is worth of investigation due to the direct photoanode functionality of both bare Hematite and doped counterpart in terms of PEC water oxidation and matching of valence band edge position with water oxidation potential [18]. Note that we have no evidence any band alignment of Hematene to electrolyte energy level. It will be a subject of further study. Here, our goal is to see any difference of photoelectrochemical response of this Hematene flakes containing photoanode from that of Hematite film. For the same, we have measured the photocurrent density of both before (B.S.) and after ultrasonicated Hematite films (A.S.) in 1M KOH, using a three-electrode configuration. The linear sweeping current Vs. Potential ($I-V$) scans were performed in both dark and under the white LED light (AM 1), and the curve obtained is shown in Figure 8 A. The plot here depicting comparison between the light and dark current densities for the thin film before sonication (B.S.) and after sonication (A.S.). In all photocurrent density patterns, the usual photocurrent plateau has not been observed as mostly been seen for nanostructured Hematite. In this case, the Hematite from which Hematene flakes are exfoliated is the direct conversion of Akagenite, crystal which usually results in more resistive action, while doped Hematite already well established to show higher photocurrent density [44]. Despite not having a Plateau-like feature, the photocurrent density of film A.S is higher than that of B.S. and displayed a photocurrent density of $50\mu\text{A}/\text{cm}^2$. Here, photocurrent density of bare Hematite film before sonication is very low in the order of $30\mu\text{A}/\text{cm}^2$ at 0.6 V. The slight increase in photocurrent density can be attributed to the more opening of pore size in the photoanode materials of A.S. due to the ultrasonication process. It is evident from the morphology discussion with FESEM study, which shows a rougher surface after the ultrasonication process on new Hematite film. At the same time, the dark current density for A.S. is lower than that of B.S. It is evident as from our earlier studies it is evident that the Hematite films show considerable dark current density due to the presence of Fe^{2+} site which on electrochemical oxidation result in extra electrons with a direct effect of Faradaic current density in the dark condition [41]. While in the A.S. film, as the ultrasonication process removes surface layers as exfoliated one, so the dark current density will be lower. The photocurrent density mentioned here is also tremendously not that high, but at least the ultrasonication process leads to a better photocurrent density which is a new finding in this domain. We believe the direct role of Hematene flakes in the overall photocurrent density can affect due to the

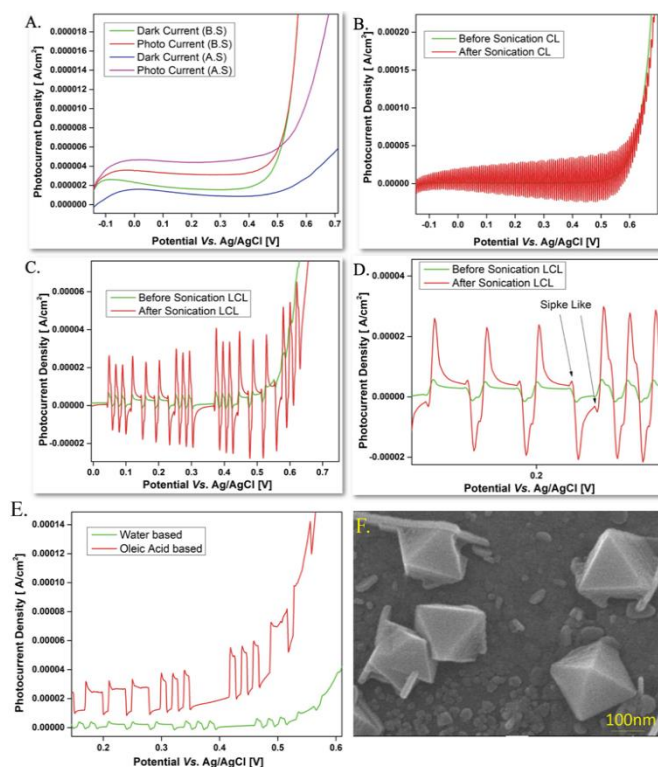


Figure 8: A. Photocurrent density comparison between Hematite films before and after ultrasonication. B. The transient chopped light current density of Hematite films obtained before and after ultrasonication; C. Limited chopped light current density of Hematite films before and after the ultrasonication process; D. Expanded chopped light current density profile shows different peak before the decay towards the cathodic direction. E. Comparison of the chopped light current densities of Hematite films obtained by both water and oleic acid-based synthesis processes. F. FESEM image of a hematite nano octahedron film showing here as a reference for the transient photocurrent density result.

maximum absorbance shown by these flakes followed by the A.S. film absorbance is higher than that of B.S. Besides these, Hematene also shows extra panchromatic light-harvesting above 550 nm and the extra increase in the photocurrent density is due to the collective action of the same. Besides these, the IPCE (incident photon to current conversion efficiency) of Hematene coated TiO_2 photoelectrode shows increase efficiency in this region [22]. However, these ultrasonication methods will give rise to more efficient photoanodes which are already well established. So, we keep it as the next objective for our future study with this new material.

A qualitative understanding of the charge transfer process from the transient photocurrent density

Does the next question arise how Hematene flakes containing film (A.S.) shows its photoinduced charge transfer action in comparisons to classic Hematite film? The underlying physical phenomena for the same need to be understood. Here, we have carried out the transient photocurrent density study of films (A.S. and B.S.) under light ON-OFF configuration and results are shown in Figure 8 B. If we consider the light ON part of the resultant data, the photocurrent density is considerably high for A.S. film than that of B.S. Also, the spike spreads across both anodic and cathodic directions. The enhancement of both the anodic and cathodic spike intensity signifies that on the surface and bulk of both the A.S. and B.S. excitonic recombination takes

place, as revealed by the spike formation. If we carefully observe at 0.4 V, the intensity of this spike in the anodic direction is more than that of the cathodic direction.

In comparison, it is remaining same for both cases for pristine Hematite film. Now, if we consider the 2D Hematene structure, the surface oxygen defect is more as validated by XPS study as described above [Figure 7 C and D]. Also, an operando synchrotron study by Braun et al. reveals that the formation of the hole for O2p band or charge transfer band is getting its maximum contribution on the photocurrent density at 0.4 V [47]. So, from here, we can justify that increase in the magnitude of spike formation in the anodic direction at 0.4 V is nothing but the function of oxygen ligand presents partially in 2D Hematene flakes followed by rest of oxygen ligands in the entire Hematite film after ultrasonication, which contributes to the formation of the hole and subsequent recombination. However, the experimental finding of the same is not done yet. We here qualitatively propose a suggested physicochemical mechanism. The photocurrent density reaches around 50 $\mu\text{A}/\text{cm}^2$ at the light - ON mode, while it relaxes back to the zero current during the light - OFF mode. The presence of cathodic transient spike is due to the bulk electron-hole recombination [48] while this is a direct first kind of study with Hematene. Next, we have plotted the comparative limited chopped light current density profile of both films, as shown in Figure 8 C. Here *limited* stands for the slow speed of the shutter, which is embedded in the light source. The result obtained leads to the observation of a quite interesting pattern, which shows an unusual transient spike on light - OFF mode. After it, the falling transient arose again to give this additional spike, as shown in Figure 8 D. In the zoom out portion of the transient photocurrent data [Figure 8 D], we have observed a different trend in the photocurrent relaxation phenomena for exfoliated materials (A.S.) in both anodic and cathodic directions. Here, we see that current density decayed in a delayed response. Before light - OFF mode, the photocurrent excited for a while forming an additional spike, till it reaches the equilibrium and again falls towards the cathodic direction. Similarly, during the light- ON step, the photocurrent rises with a delayed intermediate response in the cathodic regime, before it reaches the maximum magnitude in the anodic region. If we compare the same with the film without ultrasonication (B.S.), we can also see such a trend in the transient photocurrent density.

Regarding the photoinduced charge transfer effect, the basic understanding and observation of a transient photocurrent spike are first to need to be understood. As described elsewhere [49, 50], the photocurrent transient spike reaches a peak in the upward direction followed upon by decay to the steady-state, when light is turned on. Just after 10 sec of photon illumination if the light is turned off, the zero current occurs and again re-spiking when the light turned back on again. The physical significance of the falling photocurrent density is the conduction band electrons rapid removal into the bulk, and spike formation takes place due to the recombination of electron holes by the surface state. The sub- spike feature, we discussed above is assigned as a subsurface state generated peak. Now coming back to our discussion about the transient

photocurrent characteristic of A.S and B.S Hematite film, we have noticed that the light chopping with faster interval (figure 8 B) does not show this sub spike feature. Only when the light chopping speed is slow with longer interval, this specific feature is observed. During this, the usual falling transient decays signifies the more rapid removal of C.B. electrons into the bulk which is also apparent in this case, but the extra spike points towards slow removal of electrons, and in other words, it shows back-reaction: the recombination of electrons and holes with sub-surface states. Suppose we see the overall photocurrent density comparison, its higher than the non- exfoliated one. The Hematene flakes can acts as an extra sub-surface state while delaying the falling current while increasing the photocurrent density. The exact energy band level understanding needs further spectroscopic investigation, which will be addressed in a separate study. The falling transient also shows the photogeneration of OH • radical or an electron acceptor. If it is the case, the electron-accepting species or OH• radical concentration will be low due to which, it shows an extra spike with reverted again. The presence of an extra spike with enhanced intensity decouples the Hematene contribution from the overall photocurrent density performance.

Finally, the extra spike is absent in other Hematite nanostructured film. It is evident when we compare the transient photocurrent density [Figure 8 E] of a nano octahedron dispersed Hematite film. It is obtained from precursor dip-coating synthesized by an oleic acid route [Figure 8 F]. We have not observed such a trend in the formation of an extra spike in the transient chopped photocurrent density. From here, it is evident that the precursor chemistry leads to two different types of Hematite film with changes in the surface electronic and atomic structure as reveals by the formation of the different peak which we proposed to the formation of sub-surface state for a qualitative understanding. However, to get detail insight into the initial claim of surface and atomic structure changes, we need to do synchrotron XRD and XAS, which is for the time being out of scope due to COVID-19 constraint. Our goal is to report here only the formation of Hematene sheet and flakes with its photoelectrochemical properties. Also, the Hematene formation for oleic acid-derived Hematite nano octahedron has not been studied. However, it will be the subject of further study.

Conclusions

The exfoliation of Hematene from Hematite nanoparticle and film within a concise time scale has been demonstrated. The confirmation of the same is validated with the HRTEM study of the single Hematene layer, where it shows a symmetrical hexagonal pattern resembling honeycomb lattice of Graphene. Followed by this, a detail atomic structure understanding with the d-spacing calculation reveals that the Hematene formed is originated from the Hematite as it also shows the crystallographically more exposed (104) plane. Based on the same, its formation mechanism is proposed and predictive that due to the high surface energy of (104) planes, hydroxylation is faster due to more reactive surface. At the same time, alcohol

binding will be faster, and a hydroxyl group is incorporated between two iron atoms, which allows the easy removal of Hematene layer. The 2D shape confirms the formation of Hematene flakes for its light-harvesting property, and its origin is mostly Hematite as reveals by the EDX mapping showing only Fe and O distribution. The AFM validates the change in surface roughness of Hematite film after ultrasonication and the optical properties of both Hematene sheet and flakes show an increase in the absorbance in the 550 - 700 nm.

In contrast, Hematite film after ultrasonication shows the same absorption profile as that of Hematene flakes. The similar type of scattering contribution controls the optical properties of Hematene flakes and sheet while the bandgap changes. Next, XRD of the ultrasonicated film shows that in Hematene film a new peak appeared at (104) plane further signifies the hydroxyl ion intercalation. The XPS study validates the usual oxygen defect signature of Hematene at 532 eV, which further confirms the enhanced photoelectrochemical functionality of the Hematite film after ultrasonication treatment and the formation of sub-surface state. The photocurrent density increased up to $50\mu\text{A}/\text{cm}^2$ for Hematene flakes containing Hematite photoanode while, the pristine shows current density up to $30\mu\text{A}/\text{cm}^2$. Though it is not a fantastic performance, the future outlook of such ultrasonic modification and making of Hematene flakes on champion photoanode will boost its efficiency further for the solar water-splitting process.

Experimental

Materials

All Chemical and solvents, used in the current study, have been procured from commercial sources and possessed 97-99% purity. Ferric (III) Chloride hexahydrate ($\text{FeCl}_3 \cdot 6\text{H}_2\text{O}$) and Urea (NH_2CONH_2) was purchased from Sigma-Aldrich. Absolute Ethanol used for washing the ochre yellow precipitate was of analytical grade and was obtained from Changshu (C.S.), while distilled water was distilled in our laboratory. For the deposition of Hematite, FTO glass slides were obtained from Ants Ceramic Limited, Mumbai, India.

Synthesis of Hematite nanoparticle and thin film:

For the synthesis of the Hematite thin film using water as a solvent, a synthetic protocol similar to previously reported literature has been employed [30, 51]. Here, 1 g of Ferric Chloride Hexahydrate and 2.2 g of urea were mixed with distilled water in a round bottom flask and was stirred at 80°C . The resultant mixture forms ochre yellow colour solution after 6 hours of the reaction. The solution was then centrifuged and washed with Ethanol. The residue obtained was dried at 70°C . Later, this mass was calcinated in the air at 500°C for 3 hours to obtain a reddish-brown colour powder, which is the characteristics colour of Hematite. FTO (Fluorine doped tin oxide) substrate was clean with isopropanol; soap water followed upon by the dip-coated in the supernatant solution to obtain thin films of the same. It was then dried and further heat-treated at 500°C for 3 hours to get the Hematite film. The thickness of the hematite film is shown in figure S3, and it is $0.95\mu\text{m}$. The roughness of the hematite film before sonication is found to be 7.6 nm. We have used the centrifugation process in the isolation of akageneite powders. We have also used the

centrifuged process in the isolation and calculation of sonicated Hematene sheet yield. It is a new amendment, as described below.

Synthesis of Hematene Sheets and Flakes containing Hematite Films

For the synthesis of Hematene sheets, Hematite nanopowders obtained are ultrasonicated for 5 min in Ethanol in a glass vial. The obtained solution is further applied for TEM characterization to confirm the presence of Hematene. The Hematene flake is formed by the ultrasonication of as obtained Hematite film for 5 min in Ethanol. The films are taken out and characterized further with FESEM to confirm the presence of Hematene flakes.

The exfoliation yield of the process is calculated by following the protocol as described elsewhere [52]. Here, the weight of the empty centrifugation tube is first taken. Then the Hematene sheet solution is centrifuged for 10 min at a speed of 10000 rpm / hr. After this, the weight of the Hematene sheet along with the tube is retaken. The difference comes out as 1 mg, which is a low exfoliation yield.

Characterization of obtained powder and thin films: The morphology and lattice imaging of Hematite nanoparticles are studied with high-resolution transmission electron microscopy (model: Thermo Scientific Talos F200S scanning / transmission electron microscope (S / TEM)). The TEM sample preparation was done with the dispersion of nanoparticle in Ethanol with an ultrasonication for 5 min followed by drop cast on TEM grid drying the same to evaporate the Ethanol in an Eppendorf tube. This result in Hematene sheets like morphology, which is further studied with the same TEM model with higher resolution. The FESEM and XRD of Hematite nanoparticles are studied with Field Emission Scanning Electron Microscopy (FESEM) JEOL model JSM7100F, equipped with energy dispersive X-rays (EDX) spectrometer operating at 15 keV and Powder X-Ray diffractometer (Rigaku, Ultima IV X-Ray Diffractometer, $\text{Cu K}\alpha$ radiation). The morphology and EDX mapping of the same is carried out with FESEM (same model). The optical properties of Hematite nanoparticles and thin films are studied with UV-Vis spectroscopy (Shimadzu UV-1800 UV-Vis spectrometer). The surface topography of thin films was investigated on Atomic Force Microscopy (Agilent Technologies, model 5000), in tapping mode. The phase compositions of the thin films were studied on X-ray diffractometer (XRD) Rigaku, Smartlab XRay Diffractometer model with $\text{CuK}\alpha$ radiation of wavelength 1.54 \AA in the 2θ range of 5 to 80° in parallel beam (grazing incidence) mode. The Reflectance spectra corresponding to thin films were obtained on a UV-VIS-NIR/DRS instrument Perkin Elmer, Lambda 750 in the range 190-700 nm. The emission spectra of thin films were procured from a spectrofluorometer (Horiba Jobin Yvon, FL-1039/40), with 50 W ozone free Xe source and double Czerny Turner optics having 1200 g/mm rating blazed at 500 nm. The XPS spectra were recorded by an ESCA, Kratos Analytical, Axis Supra, U.K. spectrometer equipped with $\text{AlK}\alpha$ 600W, X-ray source. The analysis software used here is Image J (Fiji TEM package) for HRTEM FFT, FESEM analysis, Dwyddion for AFM data analysis, Casa XPS for XPS core level data analysis.

Photoelectrochemical characterization. —The photocurrent density of Hematite film both before and after ultrasonication was measured in an Electrochemical Workstation from C.H. instruments, CHI660D Potentiostat model with a Potential range of -10 to 10 V and Current range of 250 mA. The measurement set up consists of the photoelectrochemical cell (custom built from Borosil) beaker having 3-electrode system configuration with 1MKOH ($\text{pH} = 13.6$) as the electrolyte. Ag/AgCl on sat. KCl and platinum wire were used as the reference and counter electrode, respectively. A LED lamp (100mW) from Tec. Inc. USA [tec light] with embedded electronic shutter option was used as the light source with an intensity of AM 1 was used to measure the photocurrent density. The transient photocurrent density is taken using the same light source using the built-in light on-off shutter option with both fast and slow interval mode.

Conflicts of interest

There are no conflicts to declare.

Acknowledgements

The author(D.K.B) acknowledge The funding received from J.U. management start-up grant: 11 (39)/17/004/2017SG to carry out this work. The Nano Mission Project “SR/NM/NS-20/2014” supported the FESEM and XRD facilities used in this study. Next, We would like to acknowledge the TEM facility of the Center for Nano and Soft Matter Sciences (CeNS), Bangalore for the HRTEM characterization followed by the Central Research Facility (CRF) for the U.V.- Vis DRS, Thin Film XRD, Atomic Force Microscopy and Fluorescence measurement. For the XPS measurement, Central Surface Analytical Facility of IIT Bombay is duly acknowledged here.

Notes and references

- 1 K. S. Novoselov, A. K. Geim, S. V. Morozov, D. Jiang, *Science* 2004, **306**, 666.
- 2 V Nicolosi, M Chhowalla M. G Kanatzidis, M. S. Strano, J. N. Coleman, Liquid exfoliation of layered materials. *Science*, 2013, **340**, 72.
- 3 M. Naguib, V. N. Mochalin, M. W. Barsoum, Y. Gogotsi, *Adv. Mater.* 2014, **26**, 992.
- 4 Akhtar, M., Anderson, G., Zhao, R., Alruqi, A., Mroczkowska, J. E., Sumanasekera, G., & Jasinski, J. B. (2017). Recent advances in synthesis, properties, and applications of phosphorene. *npj 2D Materials and Applications*, 1(1), 1–12. <https://doi.org/10.1038/s41699-017-0007-5>
- 5 A. J. Mannix, B. Kiraly, M. C. Hersam, N. P. Guisinger, *Nat. Rev. Chem.* 2017, **1**, 0014.
- 6 S. Z. Butler, S. M. Hollen, L. Cao, Y. Cui, J. A., Gupta, H. R. Gutierrez, T. F. Heinz, S. S. Hong, J. Huang, A. F. Ismach, E. Johnston-Halperin, M. Kuno, V. V. Plashnitsa, R. D. Robinson, R. S. Ruoff, S. Salahuddin, J. Shan, L. Shi, M. G. Spencer, M. Terrones, W. Windl, J. E. Goldberger, *ACS Nano* 2013, **7**, 2898.
- 7 X. Xiao, H. Song, S. Lin, Y. Zhou, X. Zhan, Z. Hu, Q. Zhang, J. Sun, B. Yang, T. Li, L. Jiao, J. Zhou, J. Tang, Y. Gogotsi, *Nat. Commun.* 2016, **7**, 11296.
- 8 M. S. Xu, T. Liang, M. M. Shi, & H. Z. Chen, *Chem. Rev.* 2013, **113**, 3766.
- 9 Ma, Y., Li, B., & Yang, S. (2018). Ultrathin two-dimensional metallic nanomaterials. *Materials Chemistry Frontiers*, 2(3), 456–457.
- 10 T. Xu, J. Zhang, Y. Zhu, J. Wang, T. Shimada, T. Kitamura, T. Zhang, *Nanoscale Horizons* 2020. doi:10.1039/d0nh00188k
- 11 A. H. Castro Neto, F. Guinea, N. M. R. Peres, K. S. Novoselov and A. K. Geim, *Rev. Mod. Phys.* 2009, **81**, 109.
- 12 Z. Sun, T. Liao, Y. Dou, S.M. Hwang, M.S. Park, L. Jiang, J.H. Kim, S.X. Dou, *Nat. Commun.* 2014, **5**, 4458.
- 13 M. J. Montgomery, N. V. Sugak, K. R. Yang, J. M. Rogers, S.A. Kube, A. C. Ratinov, J.Schroers, V. S. Batista, L. D. Pfefferle, *Nanoscale* 2020, **12**, 14549
- 14 M. Mishra, & D.M Chun. *Appl. Catal. A* 2015, **498**, 126.
- 15 H. Zeng, J. Li, J. P. Liu, Z. L. Wang, & S. Sun, *Nature*, 2002, **420**, 395.
- 16 J. Chen, L. Xu, W. Li, & X. Gou, *Adv. Mater.* 2005, **17**, 582.
- 17 D. K. Bora, P. Deb, *Nanoscale Res Lett.* 2009, **4**, 138.
- 18 D.K. Bora, A. Braun, E.C. Constable. *Energy Environ. Sci.*, 2013, **6**, 407.
- 19 M. Gong, Y. Li, H. Wang, Y. Liang, J. Z. Wu, J. Zhou, J. Wang, T. Regier, F. Wie, H. Dai, *J. Am. Chem. Soc.* 2013, **135**, 8452.
- 20 J. H. Bang, K. S. Suslick, *Adv. Mater.* 2010, **22**, 1039.
- 21 D. K. James, J. M. Tour *Acc. Chem. Res.* 2013, **46**, 12307.
- 22 A. P. Balan, S. Radhakrishnan, C. F. Woellner, S. K. Sinha, L. Deng, C. De Los Reyes, B. M. Rao, M. Paulose, R. Neupane, A. Apte, V. Kochat, R. Vajtai, A. R. Harutyunyan, C. W. Chu, G. Costin, D. S. Galvao, A. A. Marti', P. A. Van Aken, O. K. Varghese, C. S. Tiwary, A. M. M. R. Lyer and P. M. Ajayan, *Nat. Nanotechnol.*, 2018, **13**, 602.
- 23 R. I.Gonzalez, J. Mella, P. Diaz, S. Allende, E. E. Vogel, C. Cardenas, F. Mu *2D Mater.* 2019, **6**, 045002
- 24 A. Bandyopadhyay, N. C. Frey, D. Jariwala, & V. B. Shenoy *Nano Lett.* 2019, **19**, 7793–7800.
- 25 D. Chen, G. Zhang, W. Sun, J. Li, Z. Cheng, Y. Wang, *Phys. Chem. Chem. Phys.* 2019, **21**, 12301–12309
- 26 Z. Zhang, D. Vieira, J. E. Barralet & G. Merle, *2D Mater.* 2020, **7**, 025044
- 27 B. Mohanty, Y. Wei, M. Ghorbani-Asl, A. V. Krasheninnikov, P. Rajput, B. K. Jena, *Journal of Materials Chemistry A* 2020, **8**, 6709-6716
- 28 N. Mahmood, I. Alves De Castro, K. Pramoda, K. Khoshmanesh, S. K. Bhargava & K. Kalantar-Zadeh, *Energy Storage Mater.*, 2019, **16**, 455
- 29 A. K. Patra, S. K. Kundu, A. Bhaumik, D. Kim, *Nanoscale* 2016, **8**, 365–377
- 30 The iron oxides: Structure, properties, reaction, occurrences and uses, R.M. Cornell, U. Schwertmann, 2013, Wiley VCH-Verlag GmbH and Co, Weinheim
- 31 J. K., Bailey, C. J. Brinker, & M. L. Mecartney, *Journal of Colloid & Interface Science* 1999, **157**, 1.
- 32 Y. Song, T. Liu, M. Li, B. Yao, T. Kou, D. Feng, F. Wang, Y. Tong, X. X. Liu, & Y. Li, *Adv. Energy Mater.*, 2018, **8**, 1801784.
- 33 Fan H, Song B, Liu J, Yang Z, Li Q. *Materials Chemistry and Physics*. 200, **89**, 321.
- 34 P. F. Barbosa, L. Lagoeiro, *Am. Mineral.*, 2010, **95**, 118–125.
- 35 J. Zhao, F. E. Huggins, Z. Feng, G. P. Huffman, *Clay Clay Miner.* 1994, **42**, 737-746.
- 36 Nicholas J. Reeves and Stephen Mann, *J. Chem. Soc., Faraday Trans.*, 1991,**87**, 3875.
- 37 W. C. Mackrodt, *Phys. Chem. Miner.* 1988, **15**, 228.
- 38 Y. Shinohara, H. Satozono, T. Nakajima, S. Suzuki, & S. Mishima, *J. Chem. Softw.* 1998, **4**, 41–50.
- 39 J. Y. Ni, P. S. Wang, J. L. Lu & H. J. Xiang, *Phys. Rev. Lett.* 2019, **122**, 1–5.
- 40 P. Agarwal, & D. K. Bora, *J. Electrochem. Soc.* 2019, **166**, H541.

- 41 D. K. Bora, A. Braun, R. Erni, G. Fortunato, T. Graule, E. C. Constable, *Chem. Mater.* 2011 **23**, 2051–2061
- 42 J. H. Kennedy, K. W. Frese, *J. Electrochem. Soc.*, 1978, **125**, 709.
- 43 Y. P. He, Y. M. Miao, C. R. Li, S. Q. Wang, L. Cao, S. S. Xie, G. Z. Yang, B. S. Zou, and C. Burda, *Phys. Rev. B* **71**, 125411.
- 44 B. Gilbert, J. E. Katz, J. D. Denlinger, Y. Yin, R. Falcone and G. A. Waychunas, *J. Phys. Chem. C* 2010, **114**, 50, 21994–22001
- 45 Chun-Jern Pan, Chunze Yuan, Guanzhou Zhu, Qian Zhang, Chen-Jui Huang, Meng-Chang Lin, Michael Angell, Bing-Joe Hwang, Payam Kaghazchi, and Hongjie Dai, *PNAS*, **115**, 5670–5675.
- 46 J. E. N. Swallow, B. A. D. Williamson, T. J. Whittles, M. Birkett, T. J. Featherstone, N. Peng, A. Abbott, M. Farnworth, K. J. Cheetham, P. Warren, D. O. Scanlon, V. R. Dhanak, and T. D. Veal, *Adv. Funct. Mater.* **2018**, **28**, 1701900.
- 47 A. Braun, K. Sivula, D. K. Bora, J. Zhu, L. Zhang, M. Grätzel, J. Guo, E. C. Constable, *J. Phys. Chem. C* 2012, **116**, 16870.
- 48 H. Dotan, K. Sivula, M. Grätzel, A. Rothschild, and S. C. Warren, *Energy Environ. Sci.*, 2011, **4**, 958.
- 49 D. K. Bora, E. A. Rozhkova, K. Schrantz, P. P. Wyss, A. Braun, T. Graule, E. C. Constable, *Adv. Funct. Mater.* 2012, **22**, 490–502.
- 50 C. M. Eggleston, A. J. A. Shankle, A. J. Moyer, I. Cesar, and M. Grätzel, *Aq Sci*, 2009, **71**, 151.
51. S. Zhou, J. Li, K. D. Gilroy, J. Tao, C. Zhu, X. Yang, X. Sun, and Y. Xia, *ACS nano*, 2016, **10**, 9861.
52. Arup Ghorai, Samit K. Ray, and Anupam Midya, *ACS Appl. Nano Mater.* 2019, **2**, 1170–1177.